Effects of non-uniform viscosity and entropy diffusivity on differential rotation in convecting spherical shells

Parag Gupta, David MacTaggart & **Radostin D. Simitev**

School of Mathematics and Statistics, University of Glasgow, UK

2024-09-13

"Stellar Convection 2024", NORDITA Stockholm

Introduction

- Many solar magnetic phenomena have their origin in the processes of convection within the solar interior.
- Numerical simulations are helpful for understanding solar dynamics.
- But disparities persist between observed and simulated differential rotation and convective velocities.
- Objective of talk: Compare a set of simulations with radially uniform/non-uniform viscosity and entropy diffusivity.

Introduction

- Many solar magnetic phenomena have their origin in the processes of convection within the solar interior.
- Numerical simulations are helpful for understanding solar dynamics.
- But disparities persist between observed and simulated differential rotation and convective velocities.
- Objective of talk: Compare a set of simulations with radially uniform/non-uniform viscosity and entropy diffusivity.

Introduction

- Many solar magnetic phenomena have their origin in the processes of convection within the solar interior.
- Numerical simulations are helpful for understanding solar dynamics.
- But disparities persist between observed and simulated differential rotation and convective velocities.
- Objective of talk: Compare a set of simulations with radially uniform/non-uniform viscosity and entropy diffusivity.

Outline

Discrepancies in convective structures and velocities

- The conveyor belt of Busse banana cells (aka Taylor columns, thermal Rossby waves, giant cells)

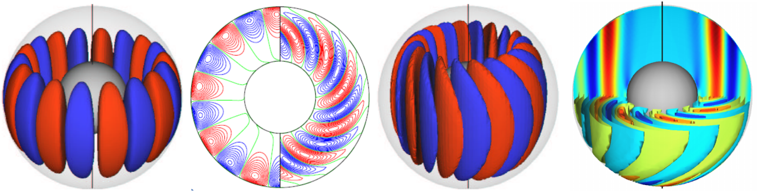

- Busse columns arise as a way to satisfy the main constraint on convection in rotating systems - the Taylor-Proudmann theorem.
- Modified by boundaries, Rossby number values, etc... but always there.
- Columns/giant cells have not been found in observations!

Discrepancies in convective structures and velocities

- The conveyor belt of Busse banana cells (aka Taylor columns, thermal Rossby waves, giant cells)

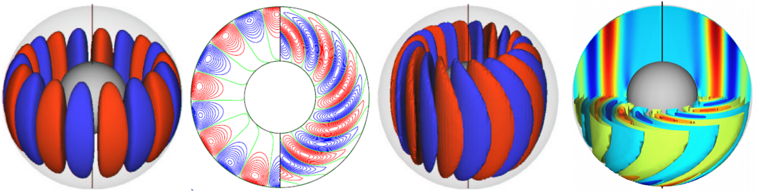

- Busse columns arise as a way to satisfy the main constraint on convection in rotating systems - the Taylor-Proudmann theorem.
- Modified by boundaries, Rossby number values, etc... but always there.
- Columns/giant cells have not been found in observations!

Discrepancies in convective structures and velocities

- The conveyor belt of Busse banana cells (aka Taylor columns, thermal Rossby waves, giant cells)

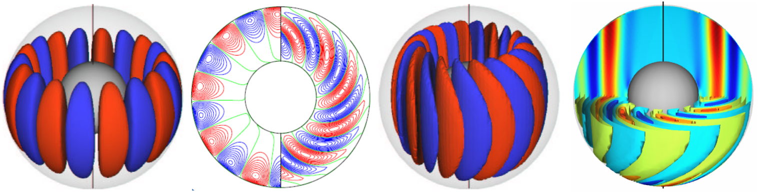

- Busse columns arise as a way to satisfy the main constraint on convection in rotating systems - the Taylor-Proudmann theorem.
- Modified by boundaries, Rossby number values, etc... but always there.
- Columns/giant cells have not been found in observations!

Discrepancies in differential rotation

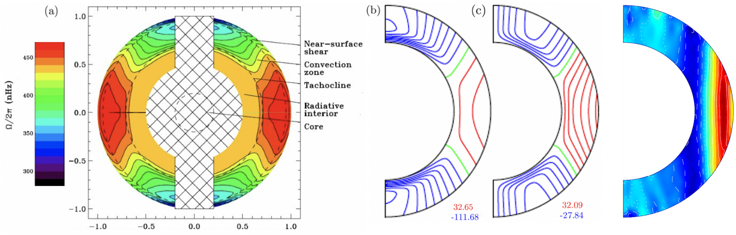

Figure 1: Time- and azimuthally-profiles of solar diff rotation.

(a) Ω – Observations of solar angular velocity (Howe 2009)

(b) $(\Omega - \Omega_\odot)$ – Solar angular velocity relative to Carrington rot (Kosovichev 1996)

(c) $u_\varphi = r \sin\theta(\Omega - \Omega_\odot)$ – Solar zonal velocity for comparison with simulations.

(d) $\langle u_\varphi \rangle_t = r \sin\theta(\Omega - \Omega_\odot)$ – Typical simulation of zonal velocity (Simitev et al. 2015)

- Observations: "conical" profile.
- Simulations: geostrophic profile.
- Differential rotation is a key ingredient in the dynamo process (via Ω-effect).
- Inaccurate differential rotation leads to questionable solar dynamo models.

Discrepancies in differential rotation

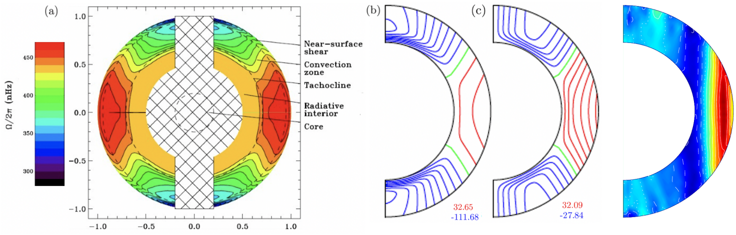

Figure 1: Time- and azimuthally-profiles of solar diff rotation.

(a) Ω – Observations of solar angular velocity (Howe 2009)

(b) $(\Omega - \Omega_{\odot})$ – Solar angular velocity relative to Carrington rot (Kosovichev 1996)

(c) $u_{\varphi} = r \sin\theta(\Omega - \Omega_{\odot})$ – Solar zonal velocity for comparison with simulations.

(d) $\langle u_{\varphi} \rangle_t = r \sin\theta(\Omega - \Omega_{\odot})$ – Typical simulation of zonal velocity (Simitev et al. 2015)

- Observations: "conical" profile.
- Simulations: geostrophic profile.
- Differential rotation is a key ingredient in the dynamo process (via Ω-effect).
- Inaccurate differential rotation leads to questionable solar dynamo models.

Discrepancies in differential rotation

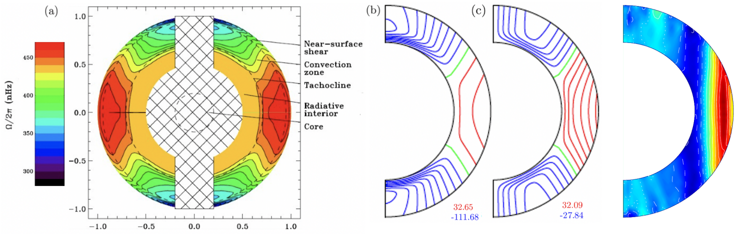

Figure 1: Time- and azimuthally-profiles of solar diff rotation.

(a) Ω – Observations of solar angular velocity (Howe 2009)

(b) $(\Omega - \Omega_\odot)$ – Solar angular velocity relative to Carrington rot (Kosovichev 1996)

(c) $u_\varphi = r \sin\theta(\Omega - \Omega_\odot)$ – Solar zonal velocity for comparison with simulations.

(d) $\langle u_\varphi \rangle_t = r \sin\theta(\Omega - \Omega_\odot)$ – Typical simulation of zonal velocity (Simitev et al. 2015)

- Observations: "conical" profile.
- Simulations: geostrophic profile.
- Differential rotation is a key ingredient in the dynamo process (via Ω-effect).
- Inaccurate differential rotation leads to questionable solar dynamo models.

Discrepancies in differential rotation

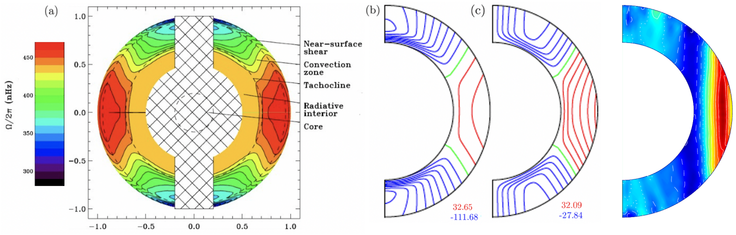

Figure 1: Time- and azimuthally-profiles of solar diff rotation.

(a) Ω – Observations of solar angular velocity (Howe 2009)

(b) $(\Omega - \Omega_{\odot})$ – Solar angular velocity relative to Carrington rot (Kosovichev 1996)

(c) $u_{\varphi} = r \sin\theta(\Omega - \Omega_{\odot})$ – Solar zonal velocity for comparison with simulations.

(d) $\langle u_{\varphi}\rangle_t = r \sin\theta(\Omega - \Omega_{\odot})$ – Typical simulation of zonal velocity (Simitev et al. 2015)

- Observations: “conical” profile.
- Simulations: geostrophic profile.
- Differential rotation is a key ingredient in the dynamo process (via Ω-effect).
- Inaccurate differential rotation leads to questionable solar dynamo models.

Discrepancies in differential rotation

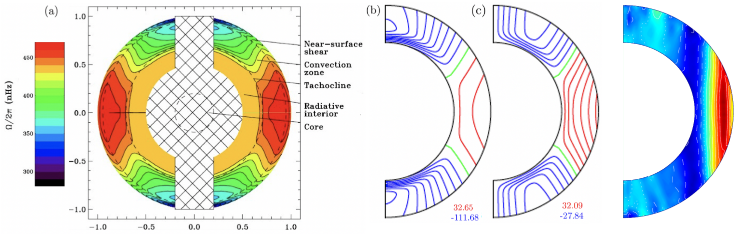

Figure 1: Time- and azimuthally-profiles of solar diff rotation.

(a) Ω – Observations of solar angular velocity (Howe 2009)

(b) $(\Omega - \Omega_\odot)$ – Solar angular velocity relative to Carrington rot (Kosovichev 1996)

(c) $u_\varphi = r \sin\theta(\Omega - \Omega_\odot)$ – Solar zonal velocity for comparison with simulations.

(d) $\langle u_\varphi \rangle_t = r \sin\theta(\Omega - \Omega_\odot)$ – Typical simulation of zonal velocity (Simitev et al. 2015)

- Observations: "conical" profile.
- Simulations: geostrophic profile.
- Differential rotation is a key ingredient in the dynamo process (via Ω-effect).
- Inaccurate differential rotation leads to questionable solar dynamo models.

Discrepancies in differential rotation

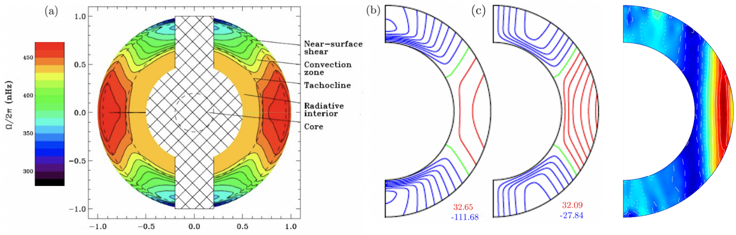

Figure 1: Time- and azimuthally-profiles of solar diff rotation.

(a) Ω – Observations of solar angular velocity (Howe 2009)

(b) $(\Omega - \Omega_\odot)$ – Solar angular velocity relative to Carrington rot (Kosovichev 1996)

(c) $u_\varphi = r\sin\theta(\Omega - \Omega_\odot)$ – Solar zonal velocity for comparison with simulations.

(d) $\langle u_\varphi \rangle_t = r\sin\theta(\Omega - \Omega_\odot)$ – Typical simulation of zonal velocity (Simitev et al. 2015)

- Observations: "conical" profile.
- Simulations: geostrophic profile.
- Differential rotation is a key ingredient in the dynamo process (via Ω-effect).
- Inaccurate differential rotation leads to questionable solar dynamo models.

Why consider non-uniform viscosity and diffusivity?

- There are very significant radial variations of material properties in the solar interior, including the convection zone.
- The radial profile of entropy diffusivity directly affects entropy distribution and this determines the local convective intensity.
- The study of linear onset of convection (Sasaki et al. 2018), appears to be the only direct investigation of effects of radially non-uniform profiles.
- The latter finds that location and shape of convection structures (columns) strongly depends on diffusivity distributions.

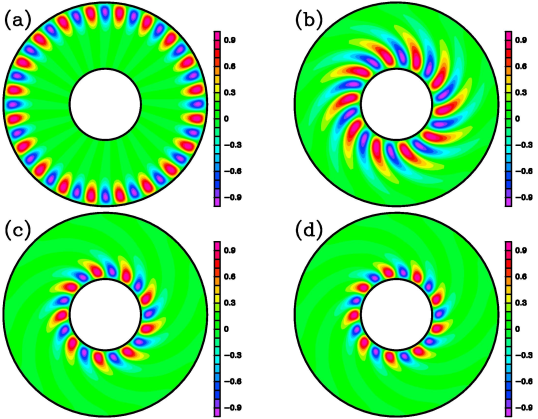

Figure 2: Radial velocity at onset for various radial distributions of entropy diffusivity in the equatorial plane. (a) uniform κ and ν. Figure courtesy (Sasaki et al. 2018).

Why consider non-uniform viscosity and diffusivity?

- There are very significant radial variations of material properties in the solar interior, including the convection zone.
- The radial profile of entropy diffusivity directly affects entropy distribution and this determines the local convective intensity.
- The study of linear onset of convection (Sasaki et al. 2018), appears to be the only direct investigation of effects of radially non-uniform profiles.
- The latter finds that location and shape of convection structures (columns) strongly depends on diffusivity distributions.

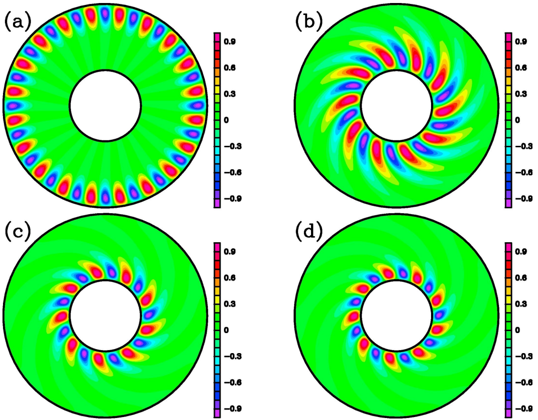

Figure 2: Radial velocity at onset for various radial distributions of entropy diffusivity in the equatorial plane. (a) uniform κ and ν. Figure courtesy (Sasaki et al. 2018).

Why consider non-uniform viscosity and diffusivity?

- There are very significant radial variations of material properties in the solar interior, including the convection zone.
- The radial profile of entropy diffusivity directly affects entropy distribution and this determines the local convective intensity.
- The study of linear onset of convection (Sasaki et al. 2018), appears to be the only direct investigation of effects of radially non-uniform profiles.
- The latter finds that location and shape of convection structures (columns) strongly depends on diffusivity distributions.

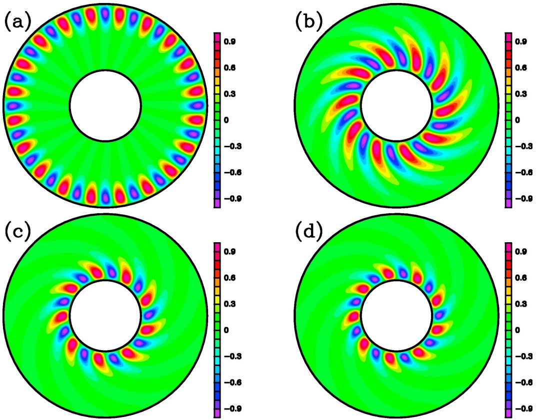

Figure 2: Radial velocity at onset for various radial distributions of entropy diffusivity in the equatorial plane. (a) uniform κ and ν. Figure courtesy (Sasaki et al. 2018).

Why consider non-uniform viscosity and diffusivity?

- There are very significant radial variations of material properties in the solar interior, including the convection zone.
- The radial profile of entropy diffusivity directly affects entropy distribution and this determines the local convective intensity.
- The study of linear onset of convection (Sasaki et al. 2018), appears to be the only direct investigation of effects of radially non-uniform profiles.
- The latter finds that location and shape of convection structures (columns) strongly depends on diffusivity distributions.

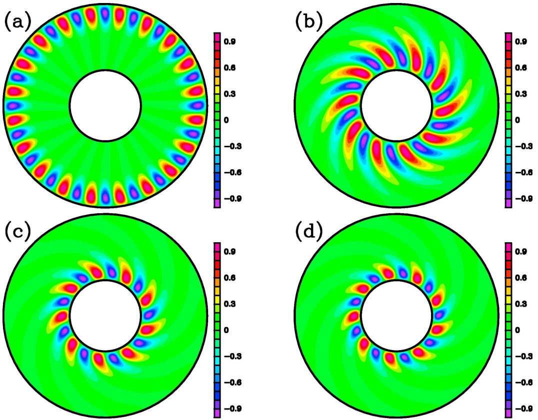

Figure 2: Radial velocity at onset for various radial distributions of entropy diffusivity in the equatorial plane. (a) uniform κ and ν. Figure courtesy (Sasaki et al. 2018).

Anelastic model of convection-driven dynamos

Setting – Electrically conducting, self-gravitating (gravity $\sim 1/r^2$), perfect gas confined to a rotating ($\Omega\hat{\boldsymbol{k}}$) spherical shell.

Background state – A hydrostatic polytropic reference state

$$\bar{\rho} = \rho_c \zeta^n, \quad \overline{T} = T_c \zeta, \quad \bar{P} = P_c \zeta^{n+1}, \quad \zeta = c_0 + c_1 d/r.$$

Scales –	Length:	$d = r_o - r_i$	Time:	d^2/ν_c	Entropy:	ΔS
	Magnetic induction:	$\nu_c\sqrt{\mu_0 \rho_c}/d$	Density:	ρ_c	Temperature:	T_c

Governing equations – Lantz-Braginsky anelastic approximation (e.g. Jones et al., 2011)

$$\nabla \cdot \bar{\rho}\boldsymbol{u} = 0, \quad \nabla \cdot \boldsymbol{B} = 0,$$

$$\partial_t \boldsymbol{u} + (\nabla \times \boldsymbol{u}) \times \boldsymbol{u} = -\nabla \Pi - \tau(\hat{\boldsymbol{k}} \times \boldsymbol{u}) + \frac{\mathrm{R}}{\mathrm{Pr}} \frac{S}{r^2} \hat{\boldsymbol{r}} + \frac{\rho_c}{\bar{\rho}} \nabla \cdot \hat{\boldsymbol{\sigma}} + \frac{1}{\bar{\rho}} (\nabla \times \boldsymbol{B}) \times \boldsymbol{B},$$

$$\partial_t S + \boldsymbol{u} \cdot \nabla S = \frac{1}{\mathrm{Pr}\bar{\rho}\overline{T}} \nabla \cdot \bar{\kappa}\bar{\rho}\overline{T}\nabla S + \frac{c_1 \mathrm{Pr}}{\mathrm{R}\overline{T}} \left(\hat{\boldsymbol{\sigma}} : \boldsymbol{e} + \frac{1}{\mathrm{Pm}\bar{\rho}} (\nabla \times \boldsymbol{B})^2 \right)$$

$$\partial_t \boldsymbol{B} = \nabla \times (\boldsymbol{u} \times \boldsymbol{B}) + \mathrm{Pm}^{-1} \nabla^2 \boldsymbol{B},$$

where the deviatoric stress tensor $\quad \hat{\sigma}_{ij} = 2\bar{\nu}\bar{\rho}(e_{ij} - e_{kk}\delta_{ij}/3), \quad e_{ij} = (\partial_i u_j + \partial_j u_i)/2.$

Anelastic model of convection-driven dynamos

Setting – Electrically conducting, self-gravitating (gravity $\sim 1/r^2$), perfect gas confined to a rotating ($\Omega\hat{\boldsymbol{k}}$) spherical shell.

Background state – A hydrostatic polytropic reference state

$$\bar{\rho} = \rho_c \zeta^n, \quad \overline{T} = T_c \zeta, \quad \bar{P} = P_c \zeta^{n+1}, \quad \zeta = c_0 + c_1 d/r.$$

Scales – Length: $d = r_o - r_i$ Time: d^2/ν_c Entropy: ΔS
Magnetic induction: $\nu_c \sqrt{\mu_0 \rho_c}/d$ Density: ρ_c Temperature: T_c

Governing equations – Lantz-Braginsky anelastic approximation (e.g. Jones et al., 2011)

$$\nabla \cdot \bar{\rho}\boldsymbol{u} = 0, \quad \nabla \cdot \boldsymbol{B} = 0,$$

$$\partial_t \boldsymbol{u} + (\nabla \times \boldsymbol{u}) \times \boldsymbol{u} = -\nabla \Pi - \tau(\hat{\boldsymbol{k}} \times \boldsymbol{u}) + \frac{\mathrm{R}}{\mathrm{Pr}} \frac{S}{r^2} \hat{\boldsymbol{r}} + \frac{\rho_c}{\bar{\rho}} \nabla \cdot \hat{\boldsymbol{\sigma}} + \frac{1}{\bar{\rho}} (\nabla \times \boldsymbol{B}) \times \boldsymbol{B},$$

$$\partial_t S + \boldsymbol{u} \cdot \nabla S = \frac{1}{\mathrm{Pr} \bar{\rho} \overline{T}} \nabla \cdot \bar{\kappa} \bar{\rho} \overline{T} \nabla S + \frac{c_1 \mathrm{Pr}}{\mathrm{R} \overline{T}} \left(\hat{\boldsymbol{\sigma}} : \boldsymbol{e} + \frac{1}{\mathrm{Pm} \bar{\rho}} (\nabla \times \boldsymbol{B})^2 \right)$$

$$\partial_t \boldsymbol{B} = \nabla \times (\boldsymbol{u} \times \boldsymbol{B}) + \mathrm{Pm}^{-1} \nabla^2 \boldsymbol{B},$$

where the deviatoric stress tensor $\hat{\sigma}_{ij} = 2\bar{\nu}\bar{\rho}(e_{ij} - e_{kk}\delta_{ij}/3), \quad e_{ij} = (\partial_i u_j + \partial_j u_i)/2.$

Anelastic model of convection-driven dynamos

Setting – Electrically conducting, self-gravitating (gravity $\sim 1/r^2$), perfect gas confined to a rotating $(\Omega\hat{\boldsymbol{k}})$ spherical shell.

Background state – A hydrostatic polytropic reference state

$$\bar{\rho} = \rho_c \zeta^n, \quad \overline{T} = T_c \zeta, \quad \bar{P} = P_c \zeta^{n+1}, \quad \zeta = c_0 + c_1 d/r.$$

Scales –

Length:	$d = r_o - r_i$	Time:	d^2/ν_c	Entropy:	ΔS
Magnetic induction:	$\nu_c\sqrt{\mu_0\rho_c}/d$	Density:	ρ_c	Temperature:	T_c

Governing equations – Lantz-Braginsky anelastic approximation (e.g. Jones et al., 2011)

$$\nabla \cdot \bar{\rho}\boldsymbol{u} = 0, \quad \nabla \cdot \boldsymbol{B} = 0,$$

$$\partial_t \boldsymbol{u} + (\nabla \times \boldsymbol{u}) \times \boldsymbol{u} = -\nabla \Pi - \tau(\hat{\boldsymbol{k}} \times \boldsymbol{u}) + \frac{\mathrm{R}}{\mathrm{Pr}} \frac{S}{r^2} \hat{\boldsymbol{r}} + \frac{\rho_c}{\bar{\rho}} \nabla \cdot \hat{\boldsymbol{\sigma}} + \frac{1}{\bar{\rho}} (\nabla \times \boldsymbol{B}) \times \boldsymbol{B},$$

$$\partial_t S + \boldsymbol{u} \cdot \nabla S = \frac{1}{\mathrm{Pr}\bar{\rho}\overline{T}} \nabla \cdot \bar{\kappa}\bar{\rho}\overline{T}\nabla S + \frac{c_1 \mathrm{Pr}}{\mathrm{R}\overline{T}} \left(\hat{\boldsymbol{\sigma}} : \boldsymbol{e} + \frac{1}{\mathrm{Pm}\bar{\rho}} (\nabla \times \boldsymbol{B})^2 \right)$$

$$\partial_t \boldsymbol{B} = \nabla \times (\boldsymbol{u} \times \boldsymbol{B}) + \mathrm{Pm}^{-1} \nabla^2 \boldsymbol{B},$$

where the deviatoric stress tensor $\quad \hat{\sigma}_{ij} = 2\bar{\nu}\bar{\rho}(e_{ij} - e_{kk}\delta_{ij}/3), \quad e_{ij} = (\partial_i u_j + \partial_j u_i)/2.$

Anelastic model of convection-driven dynamos

Setting – Electrically conducting, self-gravitating (gravity $\sim 1/r^2$), perfect gas confined to a rotating ($\Omega\hat{\boldsymbol{k}}$) spherical shell.

Background state – A hydrostatic polytropic reference state

$$\bar{\rho} = \rho_c \zeta^n, \quad \overline{T} = T_c \zeta, \quad \bar{P} = P_c \zeta^{n+1}, \quad \zeta = c_0 + c_1 d/r.$$

Scales –	Length:	$d = r_o - r_i$	Time:	d^2/ν_c	Entropy:	ΔS
	Magnetic induction:	$\nu_c\sqrt{\mu_0\rho_c}/d$	Density:	ρ_c	Temperature:	T_c

Governing equations – Lantz-Braginsky anelastic approximation (e.g. Jones et al., 2011)

$$\nabla \cdot \bar{\rho}\boldsymbol{u} = 0, \quad \nabla \cdot \boldsymbol{B} = 0,$$

$$\partial_t \boldsymbol{u} + (\nabla \times \boldsymbol{u}) \times \boldsymbol{u} = -\nabla\Pi - \tau(\hat{\boldsymbol{k}} \times \boldsymbol{u}) + \frac{\mathrm{R}}{\mathrm{Pr}}\frac{S}{r^2}\hat{\boldsymbol{r}} + \frac{\rho_c}{\bar{\rho}}\nabla \cdot \hat{\boldsymbol{\sigma}} + \frac{1}{\bar{\rho}}(\nabla \times \boldsymbol{B}) \times \boldsymbol{B},$$

$$\partial_t S + \boldsymbol{u} \cdot \nabla S = \frac{1}{\mathrm{Pr}\bar{\rho}\overline{T}}\nabla \cdot \bar{\kappa}\bar{\rho}\overline{T}\nabla S + \frac{c_1\mathrm{Pr}}{\mathrm{R}\overline{T}}\left(\hat{\boldsymbol{\sigma}} : \boldsymbol{e} + \frac{1}{\mathrm{Pm}\bar{\rho}}(\nabla \times \boldsymbol{B})^2\right)$$

$$\partial_t \boldsymbol{B} = \nabla \times (\boldsymbol{u} \times \boldsymbol{B}) + \mathrm{Pm}^{-1}\nabla^2\boldsymbol{B},$$

where the deviatoric stress tensor $\quad \hat{\sigma}_{ij} = 2\bar{\nu}\bar{\rho}(e_{ij} - e_{kk}\delta_{ij}/3), \quad e_{ij} = (\partial_i u_j + \partial_j u_i)/2.$

Anelastic model of convection-driven dynamos (cont.)

Parameters –

$$\eta = r_i/r_o, \quad n, \quad N_\rho = \ln\Big(\bar\rho(r_i)/\bar\rho(r_o)\Big), \quad \mathrm{R} = \frac{c_1 T_c d^2 \Delta S}{\nu_c \kappa_c}, \quad \mathrm{Pr} = \frac{\nu_c}{\kappa_c}, \quad \mathrm{Pm} = \frac{\nu_c}{\lambda}, \quad \tau = \frac{2\Omega d^2}{\nu_c},$$

Boundary conditions –

$$v = 0, \quad \partial_r v = 0, \quad w = 0 \quad \text{at} \quad r_i, \qquad \text{No-slip velocity BC at the bottom}$$

$$v = 0, \quad \partial_r^2 v - \frac{\bar\rho'}{\bar\rho r}\partial_r(rv) = 0, \quad \partial_r w - \frac{\bar\rho'}{\bar\rho} w = 0 \quad \text{at} \quad r_o, \qquad \text{Stress-free BC at the top}$$

$$S = 1 \quad \text{at} \quad r = r_i, \qquad S = 0 \quad \text{at} \quad r = r_o, \qquad \text{Dirichlet entropy BC}$$

$$g = 0, \quad h - h^{(e)} = 0, \quad \partial_r(h - h^{(e)}) = 0, \quad \text{at} \quad r = r_i, r_o \qquad \text{Vacuum magn BC on outside}$$

Toroidal-poloidal decomposition – Exploiting the solenoidality of the mass flux $\bar\rho\boldsymbol{u}$ and the magnetic flux $\boldsymbol{B}$,

$$\bar\rho\boldsymbol{u} = \nabla\times(\nabla\times\hat{\boldsymbol{r}}rv) + \nabla\times\hat{\boldsymbol{r}}r^2 w, \qquad \boldsymbol{B} = \nabla\times(\nabla\times\hat{\boldsymbol{r}}h) + \nabla\times\hat{\boldsymbol{r}}g.$$

Anelastic model of convection-driven dynamos (cont.)

Parameters –

$$\eta = r_i/r_o, \quad n, \quad N_\rho = \ln\Big(\bar\rho(r_i)/\bar\rho(r_o)\Big), \quad \mathrm{R} = \frac{c_1 T_c d^2 \Delta S}{\nu_c \kappa_c}, \quad \mathrm{Pr} = \frac{\nu_c}{\kappa_c}, \quad \mathrm{Pm} = \frac{\nu_c}{\lambda}, \quad \tau = \frac{2\Omega d^2}{\nu_c},$$

Boundary conditions –

$v = 0, \quad \partial_r v = 0, \quad w = 0 \quad$ at $\quad r_i,$ — No-slip velocity BC at the bottom

$v = 0, \quad \partial_r^2 v - \dfrac{\bar\rho'}{\bar\rho r}\partial_r(rv) = 0, \quad \partial_r w - \dfrac{\bar\rho'}{\bar\rho} w = 0 \quad$ at $\quad r_o,$ — Stress-free BC at the top

$S = 1 \quad$ at $\quad r = r_i, \qquad S = 0 \quad$ at $\quad r = r_o,$ — Dirichlet entropy BC

$g = 0, \quad h - h^{(e)} = 0, \quad \partial_r(h - h^{(e)}) = 0, \quad$ at $\quad r = r_i, r_o$ — Vacuum magn BC on outside

Toroidal-poloidal decomposition – Exploiting the solenoidality of the mass flux $\bar\rho \boldsymbol{u}$ and the magnetic flux $\boldsymbol{B}$,

$$\bar\rho \boldsymbol{u} = \nabla \times (\nabla \times \hat{\boldsymbol{r}} r v) + \nabla \times \hat{\boldsymbol{r}} r^2 w, \qquad \boldsymbol{B} = \nabla \times (\nabla \times \hat{\boldsymbol{r}} h) + \nabla \times \hat{\boldsymbol{r}} g.$$

Anelastic model of convection-driven dynamos (cont.)

Parameters –

$$\eta = r_i/r_o, \quad n, \quad N_\rho = \ln\Big(\bar\rho(r_i)/\bar\rho(r_o)\Big), \quad \mathrm{R} = \frac{c_1 T_c d^2 \Delta S}{\nu_c \kappa_c}, \quad \mathrm{Pr} = \frac{\nu_c}{\kappa_c}, \quad \mathrm{Pm} = \frac{\nu_c}{\lambda}, \quad \tau = \frac{2\Omega d^2}{\nu_c},$$

Boundary conditions –

$$v = 0, \quad \partial_r v = 0, \quad w = 0 \quad \text{at} \quad r_i, \qquad \text{No-slip velocity BC at the bottom}$$

$$v = 0, \quad \partial_r^2 v - \frac{\bar\rho'}{\bar\rho r}\partial_r(rv) = 0, \quad \partial_r w - \frac{\bar\rho'}{\bar\rho} w = 0 \quad \text{at} \quad r_o, \qquad \text{Stress-free BC at the top}$$

$$S = 1 \quad \text{at} \quad r = r_i, \qquad S = 0 \quad \text{at} \quad r = r_o, \qquad \text{Dirichlet entropy BC}$$

$$g = 0, \quad h - h^{(e)} = 0, \quad \partial_r(h - h^{(e)}) = 0, \quad \text{at} \quad r = r_i, r_o \qquad \text{Vacuum magn BC on outside}$$

Toroidal-poloidal decomposition – Exploiting the solenoidality of the mass flux $\bar\rho\boldsymbol{u}$ and the magnetic flux $\boldsymbol{B}$,

$$\bar\rho\boldsymbol{u} = \nabla\times(\nabla\times\hat{\boldsymbol{r}} r v) + \nabla\times\hat{\boldsymbol{r}} r^2 w, \qquad \boldsymbol{B} = \nabla\times(\nabla\times\hat{\boldsymbol{r}} h) + \nabla\times\hat{\boldsymbol{r}} g.$$

Numerical method of solution

- The anelastic code is an extension of (Tilgner, 1997; Simitev & Busse, 2005; 2009; Simitev et al., 2015).
- Toroidal-polodal decomposition into scalar unknowns v, w, h, g and S.
- Pseudo-spectral method with expansions in spherical harmonics and Chebychev polynomials.
- IMEX Crank-Nicolson scheme combined with Adams-Bashforth scheme.
- Typical resolution for these runs up to $N_r = 71$, $N_\theta = 192$, $N_\varphi = 384$.

Non-uniform profiles

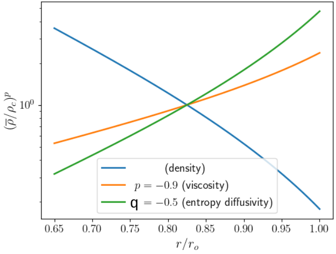

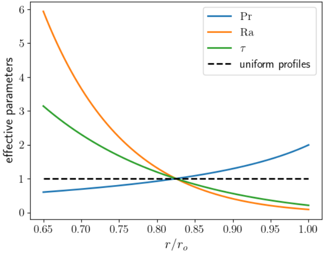

$$\overline{\nu}(r) = \nu_c \left(\frac{\overline{\rho}}{\rho_c}\right)^p,$$

$$\overline{\kappa}(r) = \kappa_c \left(\frac{\overline{\rho}}{\rho_c}\right)^q,$$

Figure 3: (left) Non-uniform viscosity and entropy diffusivity vary relative to the density. (right) Local non-dimensional parameters R, Pr and τ vary when non-uniform profiles are considered.

- Non-uniform profiles are selected to maximize the deviation from uniformity (as far as numerically feasible).
- Comparable to those used in (Brun et al. 2004, Miesch et al. 2006),
- Note, local/effective non-dimensional parameters vary with radius as a result.
- This causes radially-dependent subcriticality, and style of convection.

Non-uniform profiles

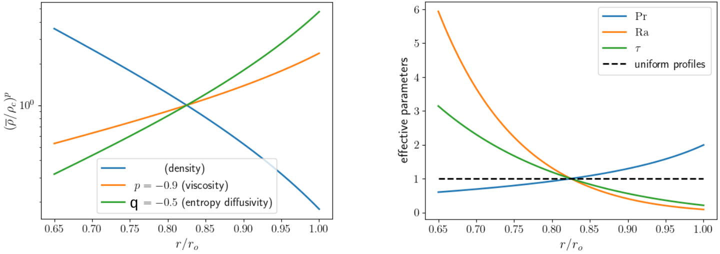

$$\overline{\nu}(r) = \nu_c \left(\frac{\overline{\rho}}{\rho_c}\right)^p,$$

$$\overline{\kappa}(r) = \kappa_c \left(\frac{\overline{\rho}}{\rho_c}\right)^q,$$

Figure 3: (left) Non-uniform viscosity and entropy diffusivity vary relative to the density. (right) Local non-dimensional parameters R, Pr and τ vary when non-uniform profiles are considered.

- Non-uniform profiles are selected to maximize the deviation from uniformity (as far as numerically feasible).
- Comparable to those used in (Brun et al. 2004, Miesch et al. 2006),
- Note, local/effective non-dimensional parameters vary with radius as a result.
- This causes radially-dependent subcriticality, and style of convection.

Non-uniform profiles

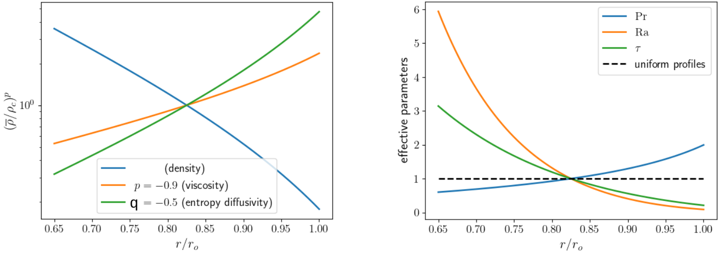

$$\overline{\nu}(r) = \nu_c \left(\frac{\overline{\rho}}{\rho_c}\right)^p ,$$

$$\overline{\kappa}(r) = \kappa_c \left(\frac{\overline{\rho}}{\rho_c}\right)^q ,$$

Figure 3: (left) Non-uniform viscosity and entropy diffusivity vary relative to the density. (right) Local non-dimensional parameters R, Pr and τ vary when non-uniform profiles are considered.

- Non-uniform profiles are selected to maximize the deviation from uniformity (as far as numerically feasible).
- Comparable to those used in (Brun et al. 2004, Miesch et al. 2006),
- Note, local/effective non-dimensional parameters vary with radius as a result.
- This causes radially-dependent subcriticality, and style of convection.

Set-up of study

Soln	r-deps	η	R	τ	P_r	N_ρ	n
A	Uniform	0.65	3×10^6	2000	0.3	3	2
B	**Non-uniform**	0.65	3×10^6	2000	0.3	3	2
C	Uniform	0.65	3×10^6	2000	1	3	2
D	**Non-uniform**	0.65	3×10^6	2000	1	3	2
E	Uniform	0.65	3×10^6	2000	5	3	2
F	**Non-uniform**	0.65	3×10^6	2000	5	3	2

Table 1: Summary of model parameter values for six selected convection solutions.

- At $\eta = 0.65$, the shell is slightly thicker than the convection zone.
- At $\tau = 2000$ the Coriolis number is moderately large.
- The density-scale height N_ρ is much smaller than for the solar convection zone.
- These choices are largely dictated by numerical considerations.

Set-up of study

Soln	r-deps	η	R	τ	P_r	N_ρ	n
A	Uniform	0.65	3×10^6	2000	0.3	3	2
B	**Non-uniform**	0.65	3×10^6	2000	0.3	3	2
C	Uniform	0.65	3×10^6	2000	1	3	2
D	**Non-uniform**	0.65	3×10^6	2000	1	3	2
E	Uniform	0.65	3×10^6	2000	5	3	2
F	**Non-uniform**	0.65	3×10^6	2000	5	3	2

Table 1: Summary of model parameter values for six selected convection solutions.

- At $\eta = 0.65$, the shell is slightly thicker than the convection zone.
- At $\tau = 2000$ the Coriolis number is moderately large.
- The density-scale height N_ρ is much smaller than for the solar convection zone.
- These choices are largely dictated by numerical considerations.

Set-up of study

Soln	r-deps	η	R	τ	P_r	N_ρ	n
A	Uniform	0.65	3×10^6	2000	0.3	3	2
B	**Non-uniform**	0.65	3×10^6	2000	0.3	3	2
C	Uniform	0.65	3×10^6	2000	1	3	2
D	**Non-uniform**	0.65	3×10^6	2000	1	3	2
E	Uniform	0.65	3×10^6	2000	5	3	2
F	**Non-uniform**	0.65	3×10^6	2000	5	3	2

Table 1: Summary of model parameter values for six selected convection solutions.

- At $\eta = 0.65$, the shell is slightly thicker than the convection zone.
- At $\tau = 2000$ the Coriolis number is moderately large.
- The density-scale height N_ρ is much smaller than for the solar convection zone.
- These choices are largely dictated by numerical considerations.

Set-up of study

Soln	r-deps	η	R	τ	P_r	N_ρ	n
A	Uniform	0.65	3×10^6	2000	0.3	3	2
B	**Non-uniform**	0.65	3×10^6	2000	0.3	3	2
C	Uniform	0.65	3×10^6	2000	1	3	2
D	**Non-uniform**	0.65	3×10^6	2000	1	3	2
E	Uniform	0.65	3×10^6	2000	5	3	2
F	**Non-uniform**	0.65	3×10^6	2000	5	3	2

Table 1: Summary of model parameter values for six selected convection solutions.

- At $\eta = 0.65$, the shell is slightly thicker than the convection zone.
- At $\tau = 2000$ the Coriolis number is moderately large.
- The density-scale height N_ρ is much smaller than for the solar convection zone.
- These choices are largely dictated by numerical considerations.

Differential rotation

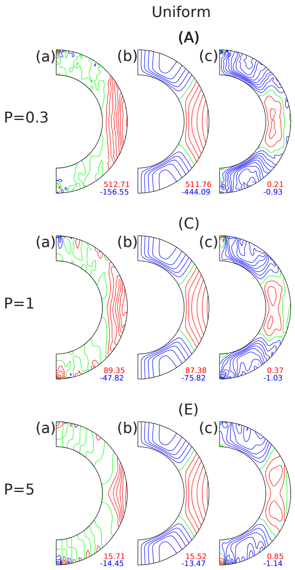

Figure 4: Differential rotation. (A – F) as in Table 1. (a) Isocontours of $\overline{u}_{\varphi}$; (b) Reference solar profile of $\overline{u}_{\varphi}$; (c) Difference between (a) and (b).

With uniform profiles:

- At small and moderate Pr and with uniform profiles, differential rotation is geostrophic outside the tangent cylinder, and small inside the tangent cylinder.
- At larger Prandtl numbers contours of zonal velocity start to deviate from a cylindrical shape but not sufficiently.

Differential rotation

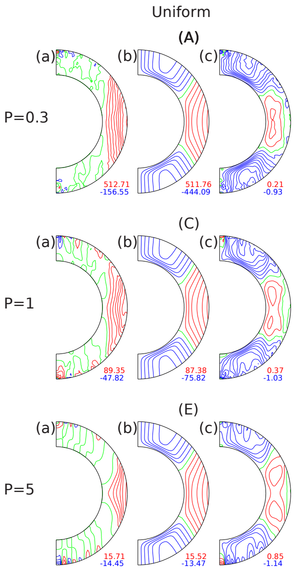

Figure 4: Differential rotation. (A – F) as in Table 1. (a) Isocontours of $\overline{u}_\varphi$; (b) Reference solar profile of $\overline{u}_\varphi$; (c) Difference between (a) and (b).

With uniform profiles:

- At small and moderate Pr and with uniform profiles, differential rotation is geostrophic outside the tangent cylinder, and small inside the tangent cylinder.
- At larger Prandtl numbers contours of zonal velocity start to deviate from a cylindrical shape but not sufficiently.

Differential rotation

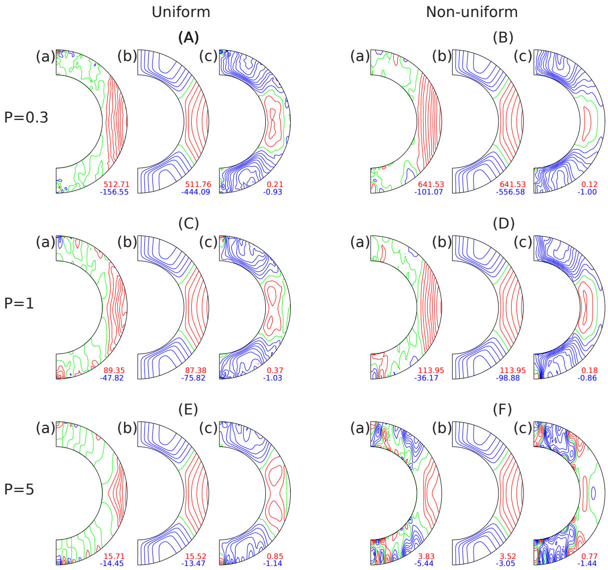

Figure 5: Differential rotation. (A – F) as in Table 1. (a) Isocontours of $\overline{u}_\varphi$; (b) Reference solar profile of $\overline{u}_\varphi$; (c) Difference between (a) and (b).

With non-uniform profiles:

- At small and moderate Pr there is little change at first.
- At larger Prandtl numbers and in the equatorial belt the contours of zonal velocity resemble observations well.
- Discrepancies remain significant in the polar regions.

Differential rotation

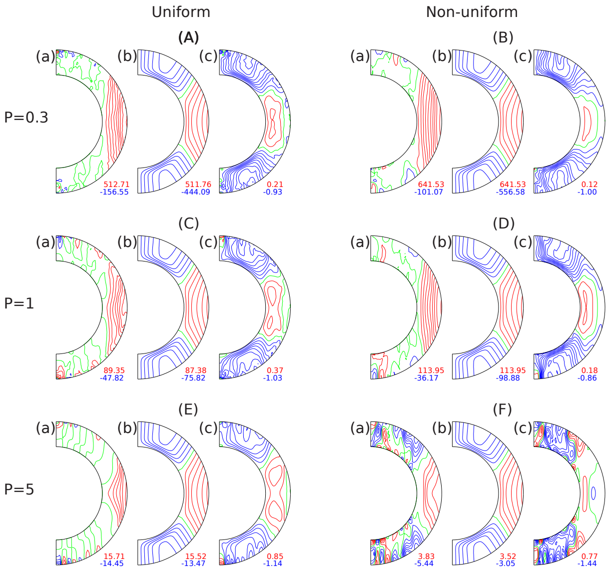

Figure 5: Differential rotation. (A – F) as in Table 1. (a) Isocontours of $\overline{u}_\varphi$; (b) Reference solar profile of $\overline{u}_\varphi$; (c) Difference between (a) and (b).

With non-uniform profiles:

- At small and moderate Pr there is little change at first.
- At larger Prandtl numbers and in the equatorial belt the contours of zonal velocity resemble observations well.
- Discrepancies remain significant in the polar regions.

Differential rotation

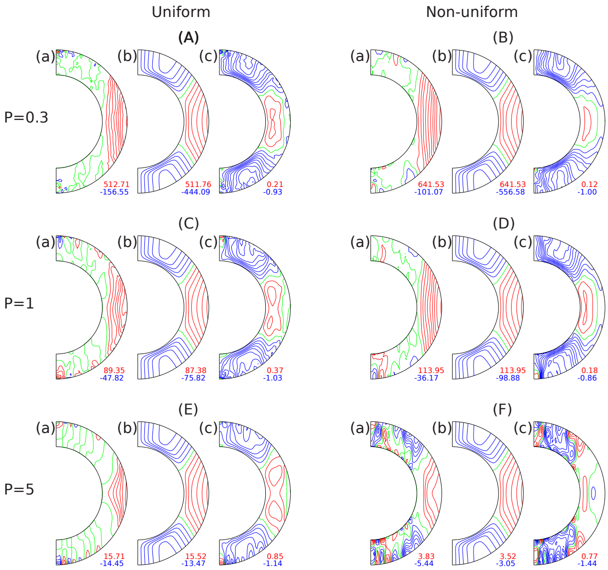

Figure 5: Differential rotation. (A – F) as in Table 1. (a) Isocontours of $\overline{u}_\varphi$; (b) Reference solar profile of $\overline{u}_\varphi$; (c) Difference between (a) and (b).

With non-uniform profiles:

- At small and moderate Pr there is little change at first.
- At larger Prandtl numbers and in the equatorial belt the contours of zonal velocity resemble observations well.
- Discrepancies remain significant in the polar regions.

Structure of convection

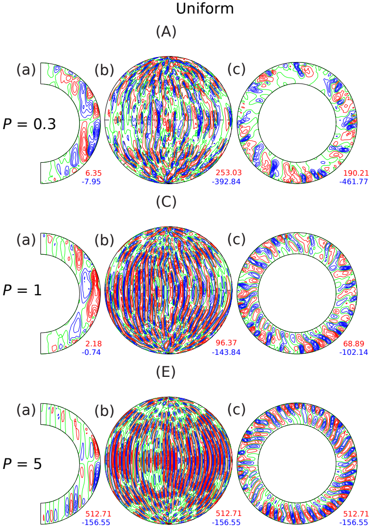

Figure 6: Flow structures corresponding to Figure 5. (a) Azimuthally-averaged meridional circulation, (b) Radial velocity at $r = 0.5$ and (c) Poloidal streamlines in equat plane.

With uniform profiles:

- Outside the tangent cylinder: thermal Rossby waves; drift in prograde direction.
- Convection in equatorial region intensifies with increase of Pr.

Structure of convection

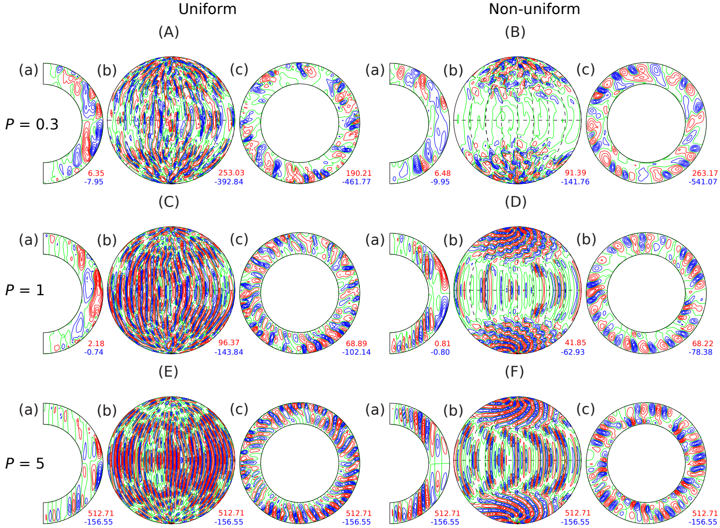

Figure 7: Flow structures corresponding to Figure 5. (a) Azimuthally-averaged meridional circulation, (b) Radial velocity at $r = 0.5$ and (c) Poloidal streamlines in equat plane.

With non-uniform profiles:

- Inside tangent cylinder: Polar convection develops.
- At larger Pr polar convection becomes organised into thin spiralling rolls.
- Outside tangent cylinder - columnar convection is weaker. Two-cartridge belt in depth.

Structure of convection

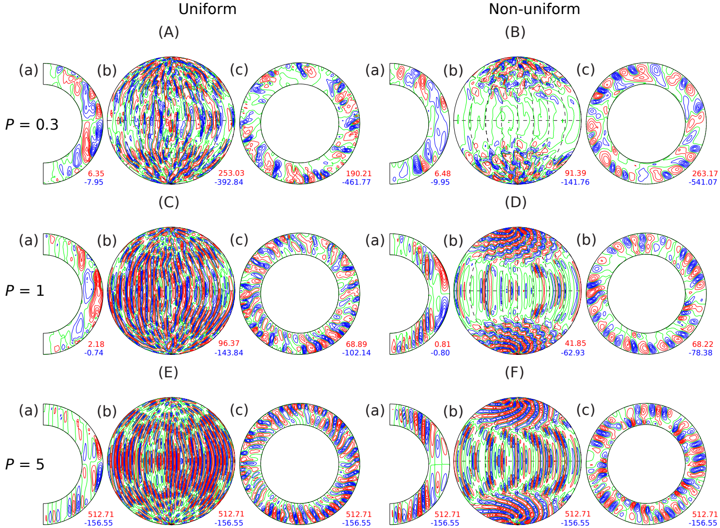

Figure 7: Flow structures corresponding to Figure 5. (a) Azimuthally-averaged meridional circulation, (b) Radial velocity at $r = 0.5$ and (c) Poloidal streamlines in equat plane.

With non-uniform profiles:

- Inside tangent cylinder: Polar convection develops.
- At larger Pr polar convection becomes organised into thin spiralling rolls.
- Outside tangent cylinder - columnar convection is weaker. Two-cartridge belt in depth.

Thermal wind balance

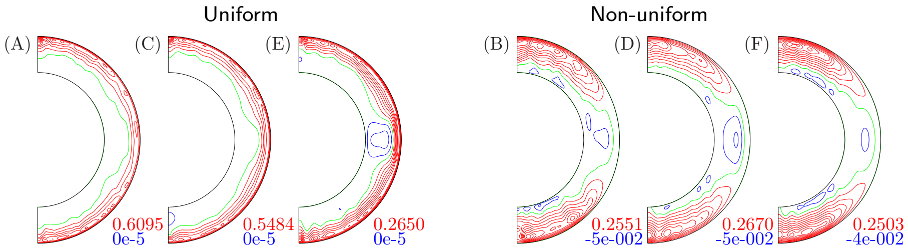

Figure 8: Azimuthally- and time-averaged entropy $\langle S\rangle_{\varphi,t}$ for uniform (A,C,E) and non-uniform (B,D,F) profiles. $\mathrm{Pr}=0.3$ (A,B), $\mathrm{Pr}=1$ (C,D), $\mathrm{Pr}=5$ (E,F). Other parameters in Table 1.

In the presence of buoyancy the Taylor-Proudmann theorem generalises to the thermal wind balance

$$\hat{\boldsymbol{k}}\cdot\nabla\langle\mathbf{u}_\varphi\rangle_t \quad\propto\quad \frac{\partial\langle S\rangle_{\varphi,t}}{\partial\theta},$$

- If $\partial\langle S\rangle_{\varphi,t}/\partial\theta\approx 0$ then the rotation profile must be close to cylindrical,
- if $\partial\langle S\rangle_{\varphi,t}/\partial\theta\neq 0$ then non-cylindrical differential rotation is promoted.

Solar–antisolar transition

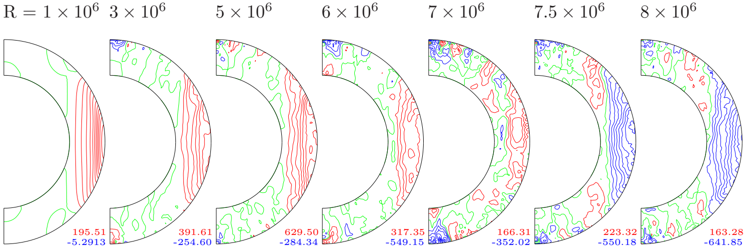

Figure 9: Differential rotation as a function of the Rayleigh number and the solar/antisolar transition. Isocontours of azimuthally averaged zonal velocity ($\overline{u}_\varphi$) are plotted for the Rayleigh number values indicated in the plot. The rest of the parameter values are specified in Table 1, with $\mathrm{Pr} = 0.3$ and uniform $\bar{\nu}$ and $\bar{\kappa}$ values.

- Transition to anti-solar rotation occurs as Rayleigh number R is increased or as Coriolis number τ is decreased.
- Transition depends on other parameters as well.

Effects of self-sustained magnetic fields

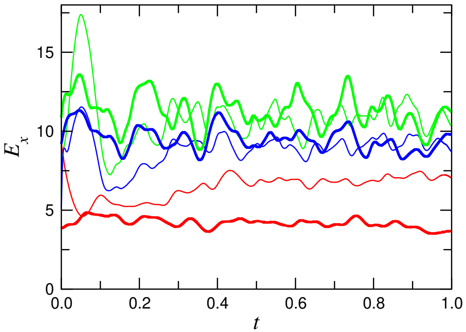

Figure 10: Time series: Dynamo (E) shown by thick lines vs. Non-magnetic convection (E') shown by thin lines) energy densities. Selected kinetic energy densities: equatorially symmetric toroidal (red), fluctuating poloidal (green), and fluctuating toroidal (blue).

- Self-sustained magnetic field affects the amplitude of differential rotation.

Effects of self-sustained magnetic fields

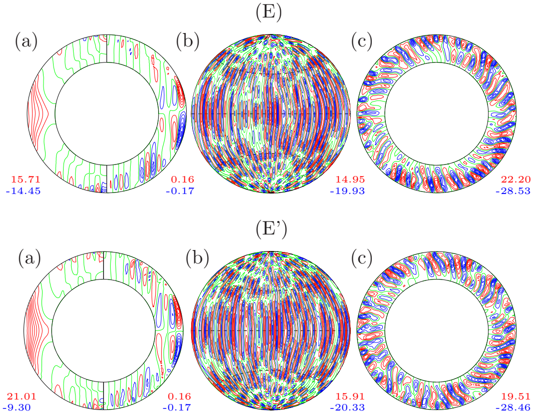

Figure 11: Comparison of dynamo (E) and non-magnetic convection (E') solutions at identical parameters.

- Self-sustained magnetic field does not affect other convective structures significantly.

Conclusion

- Radially non-uniform viscosity and entropy diffusivity profiles affect differential rotation patterns.
- Improved agreement with solar differential rotation profile at mid-latitudes for higher Prandtl numbers.
- Significant discrepancies at the polar regions.
- Future work: Expanded parameter sweeps to look for better agreement in the polar regions and for better agreement in amplitudes, using in particular fixed-flux entropy BCs.
- Future work: Analysis of dynamos.

Gupta, MacTaggart, Simitev (2023) Fluids, 8(11), 288

References

Allan Sacha Brun, Mark S Miesch, and Juri Toomre. Global-scale turbulent convection and magnetic dynamo action in the solar envelope. *The Astrophysical Journal*, 614(2):1073, 2004.

Rachel Howe. Solar Interior Rotation and its Variation. *Living Reviews in Solar Physics*, 6(1):1, December 2009. doi: 10.12942/lrsp-2009-1.

Alexander G Kosovichev. Helioseismic constraints on the gradient of angular velocity at the base of the solar convection zone. *The Astrophysical Journal*, 469(1):L61, 1996.

Mark S Miesch, Allan Sacha Brun, and Juri Toomre. Solar differential rotation influenced by latitudinal entropy variations in the tachocline. *The Astrophysical Journal*, 641(1):618, 2006.

Youhei Sasaki, Shin ichi Takehiro, Masaki Ishiwatari, and Michio Yamada. Effects of radial distribution of entropy diffusivity on critical modes of anelastic thermal convection in rotating spherical shells. *Physics of the Earth and Planetary Interiors*, 276:36–43, March 2018. doi: 10.1016/j.pepi.2017.09.003. URL `https://doi.org/10.1016/j.pepi.2017.09.003`.

Radostin D. Simitev, Alexander G. Kosovichev, and Friedrich H. Busse. Dynamo effects near the transition from solar to anti-solar differential rotation. *The Astrophysical Journal*, 810(1):80, September 2015. doi: 10.1088/0004-637x/810/1/80. URL `https://doi.org/10.1088/0004-637x/810/1/80`.